Earth and Planetary Science Letters 355–356 (2012) 213–222

Contents lists available at SciVerse ScienceDirect

Earth and Planetary Science Letters

journal homepage: www.elsevier.com/locate/epsl

An unsually large ULVZ at the base of the mantle near Hawaii

Sanne Cottaar [a,*], Barbara Romanowicz [a,b,c]

[a] Berkeley Seismological Laboratory, UC Berkeley, 215 McCone Hall 4760, Berkeley, CA 94720-4760, United States
[b] Collège de France, Paris, France
[c] Institut de Physique du Globe, Paris, France

ARTICLE INFO

Article history:
Received 8 June 2012
Received in revised form
29 August 2012
Accepted 1 September 2012
Editor: P. Shearer
Available online 13 October 2012

Keywords:
ULVZ
Pacific LLSVP
Hawaiian hotspot
Sdiff

ABSTRACT

Previous studies have documented the presence of ultra-low-velocity-zones (ULVZs) at the base of the mantle, through observations of body wave complexities. Geometrically their heights are in the range of ~5–30 km, while little is known about their lateral extent beyond about 10^2 km, due to limitations in sampling. Here we show remarkable features in the waveforms of S/Sdiff phases of western Pacific events observed at stations in North America that indicate the presence of a very large ultra-low-velocity-zone (ULVZ) at the base of the mantle, centered ~11° to the southwest of Hawaii, within and near the northern border of the Pacific LLSVP. Waveform complexities include strongly delayed (> 30 s) postcursors. Measurements of travel times, beamforming analysis of out-of-plane energy, and full waveform comparisons with 3D numerical simulations, constrain the location, lateral extent, height and velocity reduction of the ULVZ with some level of trade-off. The simplified 3D model consists of a cylindrical ULVZ with a large aspect ratio of ~20 km in height and ~910 km in diameter at the CMB. The shear wave velocity reduction is ~20%. This is to our knowledge the largest ULVZ mapped to date and the first time the lateral extent of a ULVZ has been constrained with some precision. Its location suggests that it may be the root of a long-lived, stable plume responsible for the Hawaiian volcanic chain, the hotspot track with the largest buoyancy flux.

Published by Elsevier B.V.

1. Introduction

The lowermost ~200 km of the mantle are dominated by two large antipodal regions of low shear velocities, also called 'superplumes' or large low shear velocity provinces (LLSVPs). Both are centered close to the equator, one beneath Africa and the other beneath the Pacific. LLSVPs are responsible for the strong and dominant "degree two" in global shear wave velocity models in the lowermost 1000 km of the mantle (e.g. Dziewonski et al., 2010). Local waveform studies indicate that the edges of the LLSVPs are sharp (e.g. Ni et al., 2002; To et al., 2005; Sun et al., 2009) and LLSVPs may be denser than their surroundings (Ishii and Tromp, 2004; Trampert et al., 2004), suggesting that they may be chemically distinct. In particular, it has been proposed that they might consist of primitive, non-pyrolytic material (Deschamps et al., 2011). The role of the LLSVPs in the global dynamics is still a question of debate. It is difficult to model stable super-domes (Davaille, 1999), as material tends to accumulate in more ridge-like features (McNamara and Zhong, 2004). Locations of denser material could be controlled by the forces exerted by the surrounding downwelling material (McNamara and Zhong, 2005; Tan et al., 2011; Steinberger and Torsvik, 2012), or, alternatively, the LLSVPs might represent long-lived structures that control the surrounding mantle circulation (Dziewonski et al., 2010).

Local waveform studies, which have higher resolution than global tomography, have documented the occurrence of ultra low velocity zones (ULVZs) mostly near the borders of LLSVPs. An overview map of the possible lateral extent of ULVZs based on estimates of data sensitivity kernels is given in Supplementary material of McNamara et al. (2010). The corresponding shear wave velocity reductions are in the range of −10 to −30%. To date, the documented ULVZs heights are constrained at ~5–30 km, while little is known about the lateral extent (due to data coverage). The seismic phases used to detect these structures include reflected phases (PcP, e.g. Rost et al., 2010; ScP, e.g. Rost et al., 2005), scattered core phases (SPdKS, e.g. Thorne and Garnero, 2004, SKS, e.g. Rondenay and Fischer, 2003, PKP, e.g. Luo et al., 2001, PKKP, e.g. Rost et al., 2006) and diffracted phases (Sdiff, e.g. To et al., 2011). ULVZs might also have a signature in normal mode splitting functions (Koelemeijer et al., 2012). At this point it is unclear if the variations in ULVZ geometries are due to the large uncertainties in lateral extent and trade-offs between dimension and velocity reduction in seismic studies, or if a range of ULVZs exists on the CMB. Geodynamic modeling (Bower et al., 2011) suggests a range of different ULVZs of different sizes and shapes as a function of

* Corresponding author. Tel.: +1 5105298661.
E-mail address: sanne@berkeley.edu (S. Cottaar).

0012-821X/$ - see front matter Published by Elsevier B.V.
http://dx.doi.org/10.1016/j.epsl.2012.09.005

density contrast and amount of dense material available. The cause of ULVZs is mainly thought to be iron enrichment (Wicks et al., 2010; Mao et al., 2006) and/or the presence of melt inclusions (Williams and Garnero, 1996; Hier-Majumder, 2008).

Here we present a dataset of transverse component S/Sdiff waveforms from three western Pacific events observed at stations in North America, which illuminate an unusually large ULVZ at the northern edge of the Pacific LLSVP, near Hawaii. Owing to the strong sensitivity of the data to the structure, we can forward model a simplified 3D ULVZ, and provide constraints on its geometry and strength including, for the first time, its lateral extent.

2. Data and observations

2.1. Event 1. March 20, 2010 event

The main event we considered (Event 1) is a deep earthquake (Mw 6.6; depth=414 km) which occurred on March 20, 2010 in the New Ireland Region, Papua-New Guinea (Table 1). Piercing points 40 km above the CMB as predicted for a 1D model (PREM, Dziewonski and Anderson, 1981) are plotted in map view in Fig. 1 for all S/Sdiff paths (gray circles). The USArray transportable array (http://www.iris.edu/earthscope/usarray) and numerous other broadband networks provide dense station coverage in North America. The background tomographic model shows how the paths sample the northern Pacific LLSVP boundary. The radiation pattern for SH is shown in Fig. S1 for the take-off angle of the diffracting phase. The pattern is favorable with strong SH amplitudes in the azimuthal range covered by the data.

To process the data, the seismic instrument responses are deconvolved and horizontal components are rotated to radial and tangential. Tangential component S and Sdiff waveforms for Event 1, filtered with a bandpass butterworth filter between 10 and 20 s (0.05–0.1 Hz), are shown in Fig. 2 for distance ranges of 88–94° (panel a) , 94–100° (panel b) and 100–110° (panel c). The waveforms are shifted to align with the predicted S/Sdiff arrival time for the 1D model PREM.

Waveforms for Event 1 fall into three clusters that geographically correspond to traces sampling D″ outside the LLSVP, at its boundary, and inside the LLSVP, respectively (details in Supplementary material Section 2). When waveforms are filtered between 10 and 20 s (Fig. 2a–c), it becomes apparent that, at azimuths larger than about 48°, the S/Sdiff phase is split into a weaker first arrival and a strongly delayed second phase, which we call ‘postcursor I’. The postcursor has the same polarity as the main phase. The presence and move-out of postcursor I is mainly a function of azimuth, but the amplitude ratio between postcursor I and the main phase becomes larger with increasing distance (Fig. 2b and c). The main phase amplitude for the longer periods included is less affected, but the postcursor still persists (Supplementary Fig. S2) and there is also evidence of an intermediate postcursor. For periods above 30 s the waveforms appear unaffected apart from a slight delay.

2.2. Event 2. June 12, 2003 event

A second event, which occurred 400 km to the southeast of Event 1, shows similar complexities. At that time, which was before the deployment of the USArray, the station coverage in North America was not as good. Event 2, however, did occur during the deployment of the NARS-baja array (Clayton et al., 2004), offering extended coverage towards the south. Waveforms on the tangential component are shown in Fig. 2de filtered between 10 and 20 s. This event is shallower, and thus the S(diff) and depth phases are only 80 s apart and are both shown. The sS(diff) phase has significant amplitude, while the pS(diff) cannot be distinguished. Similar postcursors as for Event 1 are visible,

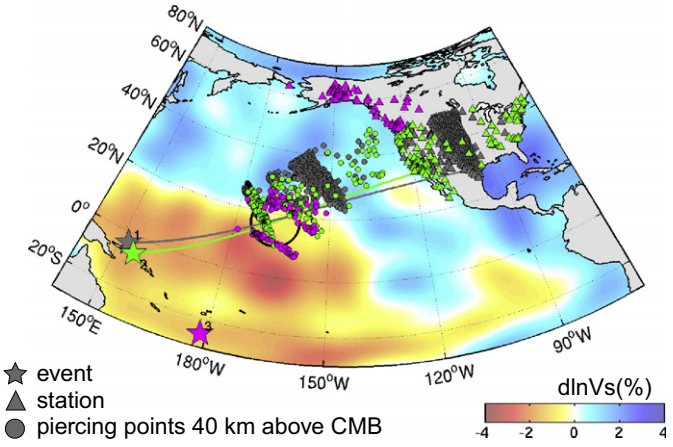

Fig. 1. Coverage of the Event 1 (gray), Event 2 (green) and Event 3 (magenta) events across the northern boundary of the Pacific LLSVP. The circles represent the entry and exit points of the Sdiff phases approximately 40 km above the CMB. Background model is SAW24B16 (Mégnin and Romanowicz, 2000) at a depth of 2750 km (~ 150 km above the CMB). Black circle shows location of the proposed ULVZ. (For interpretation of the references to color in this figure legend, the reader is referred to the web version of this article.)

Table 1
Selected CSEM models. Correlation shows mean correlation between synthetics and observed diffracted phases of Event 1 in the 10–20 s bands.

Model	Center lon (°W)	Center lat (°N)	Radius (km)	Height (km)	Vel. red. (%)	Corr.	Section
NZ	Background model: modified SAW24B16					0.42	4.2.1
ZH1	165	19	440	15	20	0.38	Height 4.2.1
ZH2, ZS2	165	19	440	25	20	0.69	Height 4.2.1, size 4.2.2
ZH3	165	19	440	35	20	0.34	Height 4.2.1
ZH4	165	19	440	45	20	0.09	Height 4.2.1
ZS1	165	19	330	25	25	0.62	Size 4.2.2
ZS3	165	19	580	25	16	0.41	Size 4.2.2
ZS4	165	19	410	25	25	0.26	Size 4.2.2
ZS5	165	19	410	25	18	0.51	Size 4.2.2
ZL1	175	13.5	455	25	20	0.34	Location 4.2.3
ZL2	170	16.5	455	25	20	0.47	Location 4.2.3
ZL3	165	19	455	25	20	0.67	Location 4.2.3
ZL4	160	21.5	455	25	20	0.69	Location 4.2.3
ZL5	155	23.5	455	25	20	0.67	Location 4.2.3
ZF1	167.5	17.5	455	25	20	0.64	Event 3
ZF2	167.5	17.5	455	20	20	0.64	Event 31

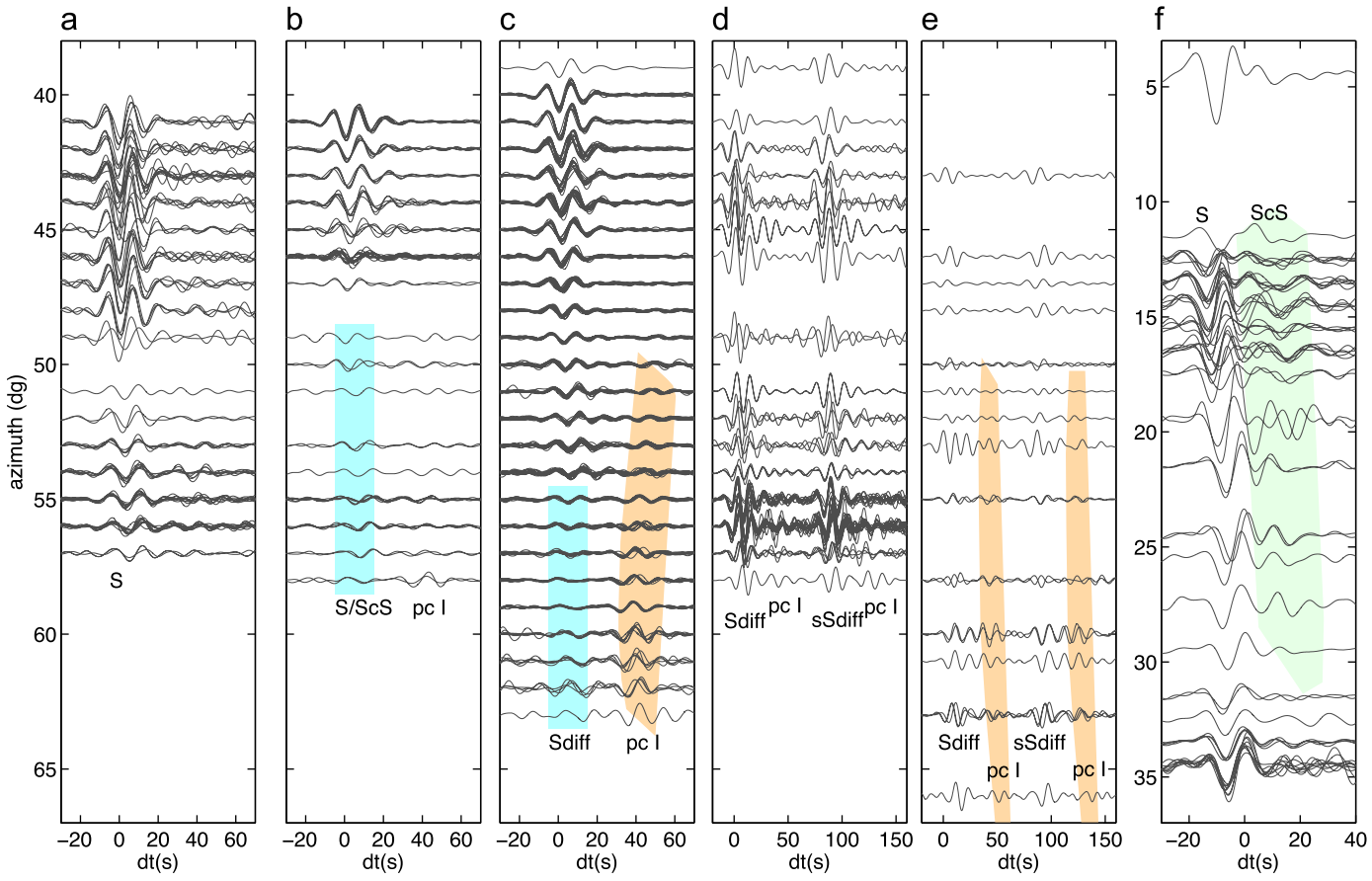

Fig. 2. Tangential velocity waveforms for Event 1 at distances between 88° and 94° (a), 94° and 100°(b), and 100° and 110° (SHdiff, c), for Event 2 between 88° and 94° (d) and 94° and 110° (e) and for Event 3 between 89° and 96° (f). Traces are plotted in azimuth bins of one degree. Data are filtered between period of 10–20 s (a–e) and 10–30 s (f). All traces within one event are normalized by the same constant. Shaded bands indicate the strongest occurrences of postcursor I in Sdiff (orange) and in ScS data (green) and the strongest distortion of the main phase (blue). Most modeling of this study is focused on fitting the 316 traces at the furthest distances of Event 1 (panel c). (For interpretation of the references to color in this figure legend, the reader is referred to the web version of this article.)

and also present an increased move-out in the delay of postcursor I towards the south. The reduction in amplitude of the main phase is not as apparent as in Event 1. Clustering analysis of these waveforms is shown in Supplementary material. This event has previously been studied by To et al. (2011) and we compare our results with their's in Section 5.

Similar complexities could in principle also be seen after the main Sdiff phase at similar azimuths for every other event we looked into. Waveforms for one other event (on September 4th 1997) are presented by To et al. (2011) along with Event 2. Coverage for this event is significantly less dense and its magnitude is smaller. Other, nearby, recent events (on 2010/08/04, 2010/08/15, 2010/12/13, 2011/02/07, 2011/12/14) since the deployment of USArray, show disappearance of the main arrival and delayed postcursor energies, but none are suitable for in-depth analysis. A number of events are too shallow (<150 km), so that the postcursor and depth phases interfere, making it difficult to analyze them. Other events are too small, or have nodal planes in the azimuthal direction of interest. During the final preparation of this paper, the most suitable event so far occurred on 2012/04/17 and confirms all the observations seen here.

2.3. Event 3. February 21, 2011 event in Fiji

We also consider a recent deep (567 km) event in the Fiji Islands from which diffracted waves to Alaska and USArray illuminate the same D″ region but from a different angle (Fig. 1, magenta). In the distance range available (89–96°), the ScS wave should arrive less than 3 s after the S phase, based on a 1D reference model. However, significant time delays in the 5–27° azimuth range (Fig. 2f) indicate that it is affected by a localized very slow anomaly, not sensed by the S wave. Some of the traces exhibit strong scattering, with at least one apparent postcursor.

3. Data analysis

3.1. Travel times

As cross-correlation measurements are unsuitable for the strongly distorted and attenuated Sdiff-phases at azimuths greater than 54°, we measure travel times by lining up the first peak of the waveform with synthetic 1D PREM reference waveforms. Results are shown in Fig. 3a. As the path enters the LLSVP, the delay in the Sdiff phase is gradual, lacking a sharp transition as observed for the African plume boundary (Ni and Helmberger, 2003; To et al., 2005). Much of the scatter in the travel times is due to distance effects. The move-out with distance is similar to that seen in SKS travel times (Fig. S5), and seems to correlate with the upper mantle structure below the US: travel times for stations in the west are generally several seconds shorter than for stations above the craton in the central US. Even though the SKS phase shows the same trends in absolute travel times with distance, it cannot be used as a suitable reference phase, as it is in general delayed by more than 5 s with respect to the Sdiff phase. We

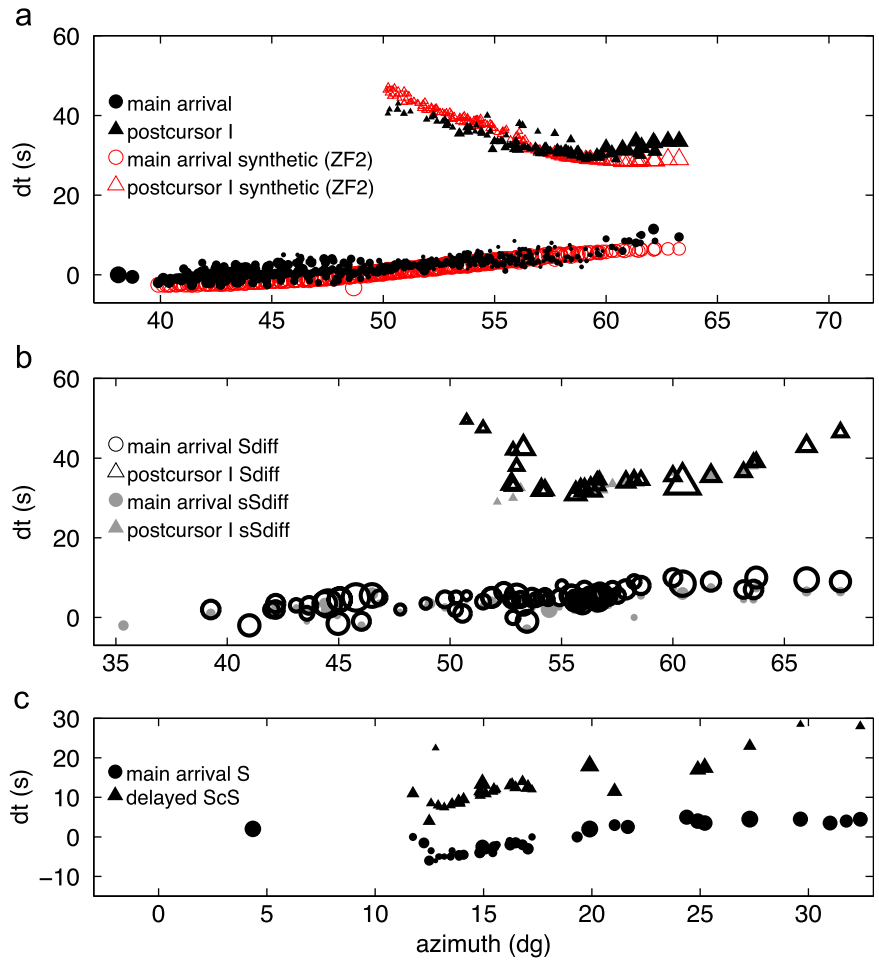

Fig. 3. Differential travel times between data and PREM synthetics measured in the 10–20 s band for main phase (circles) and postcursor (triangles). Panel (a) is observed and synthetics (ZF2) for Event 1, panel (b) for Event 2 and panel (c) for Event 3 (note that the azimuth range is very different for this last event). In Event 2 open symbols are for Sdiff, closed (gray) symbols for sSdiff. Symbol size indicates relative amplitude normalized by the amplitude of the PREM synthetic Sdiff phase.

explain this by the difference in paths of SKS and Sdiff on the source side, where the SKS phase samples a region where the Pacific LLSVP extends higher into the lower mantle (He and Wen, 2009). We avoid biases from this structure by not using SKS as a reference phase.

The travel times for postcursor I are measured manually with respect to the Sdiff waveforms in PREM synthetics. This synthetic reference phase does not match the postcursor waveforms closely at all stations, so we preferentially line up the first peak. Results are also shown in Fig. 3a. For Event 1, the minimum delay for postcursor I is around $\sim 60^\circ$ in azimuth and delays increase towards smaller azimuths. There is some indication that they also increase towards larger azimuths. Fitting the travel times with a degree 4 polynomial results in a best fitting minimum travel time delay of ~ 30 s with respect to Sdiff, at an azimuth of $\sim 60^\circ$ (shown by the gray line in Fig. 1).

For Event 2, which occurred to the southeast of Event 1, shifting observations in the US to smaller azimuths (e.g. Fig. 1), the NARS-Baja California stations (Clayton et al., 2004) provide complementary coverage at larger azimuths, showing increasing delays towards the south. Here the minimum travel time delay of postcursor I with respect to Sdiff is ~ 32 s at an azimuth of $\sim 57^\circ$ (Fig. 3b).

For Event 3, the ScS phase is delayed with respect to S (Fig. 3c). Both phases show the same trend of arriving faster between 12° and 20° azimuth. This must be due to an upper mantle effect, as the same trend is seen in other phases including SKS. In general, these observations show many other delayed scatterers that are small in amplitude.

3.2. Beamforming

The beamforming array technique (To and Capdeville, 2011) assumes that the energy comes in as a plane wave. The Sdiff phase has the advantage of having a single horizontal slowness across the entire array. The results are insensitive to the precise choice of the reference slowness, but we use 8.5 s/degree. For each station we include the closest 20 stations. Then travel times are calculated between each station and the reference station for plane waves over a range of backazimuths. The Sdiff phase is windowed, filtered between 10 and 20 s, and then stacked with the suitable travel time shifts for each of these stations. If the phases line up coherently for a specific backazimuth, the stacked waveform will be enhanced; otherwise, the phases from different stations will destructively interfere. We find the backazimuth for which the stack has the largest amplitude.

The back azimuth of the main phase is on average shifted from the great circle path by 2–3° towards more northerly directions (Fig. 4a). The shift is not due to a bias in the method, as synthetics for PREM (Dziewonski and Anderson, 1981) give the exact great circle backazimuths. It can be explained by 3D background velocity variations in the lowermost mantle, as shown by applying the same method on synthetics calculated in the model SAW24B16 (Mégnin and Romanowicz, 2000) in D″, which shows

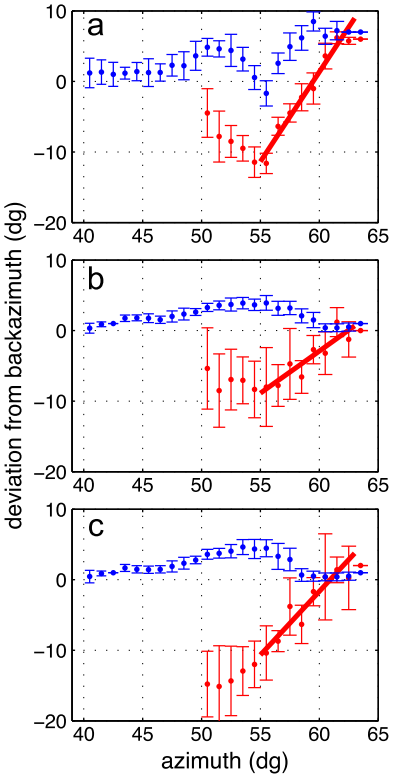

Fig. 4. Beamforming results for Event 1 in observed data (a) and synthetic data for models ZF2 (b) and ZL4 (c). Backazimuths of the arriving energy of the main phase (blue) and postcursor (red). Mean and standard deviation of the backazimuth referenced to the great circle backazimuth for stations in each azimuth bin. Error bars indicate scatter within each bin. Positive means the phase comes from further to the north. Results for the postcursors at azimuths less than 50° are not shown as they have very low amplitudes (and highly scattered results). (For interpretation of the references to color in this figure legend, the reader is referred to the web version of this article.)

a similar shift. Presumably the northern boundary of the Pacific LLSVP is causing waves to refract by several degrees towards the south. A southerly shift at the LLSVP boundary will be viewed at the station as energy arriving more from the north. At the larger azimuths, where the main phase is reduced in amplitude, there is a larger scatter in the backazimuth measurement. Energy mainly comes further from the north.

The backazimuth of the postcursor can only be measured for azimuths larger than 50° where the amplitude of the postcursor is sufficiently large. Above this azimuth, we have measurements for every station in the distance range of 100–110°. The backazimuth deviation is around zero at an azimuth of 59–60° and this corresponds approximately to the azimuths where the delays of the postcursor are minimal. At larger azimuths, the backazimuth becomes more northerly, while it is progressively more southerly at smaller azimuths. In the center of the array, around azimuths of 50–54°, the backazimuth measurements return to zero, although we find the beamforming results to be very uncertain for these smaller amplitude postcursors.

3.3. Cause of postcursor: initial modeling

Previous studies have interpreted postcursors in Sdiff phases as due to multipathing on the edge of one of the LLSVPs (To et al., 2005; Sun et al., 2009). In those studies, postcursors are less delayed and visible in a wide period band, as LLSVP boundaries extend to several hundreds of kilometers above the CMB. To produce postcursor delays of up to 47 s and to limit postcursor occurrence to periods shorter than 30 s, a causative structure with a stronger velocity reduction and smaller height is required, resembling previously modeled ULVZs.

By first considering the effects of the structure in the framework of ray theory, we show that, to first order, we can assume a circular base for this structure. In this case, we expect seismic waves to travel through the structure and be refracted by its boundaries according to Snell's law (as illustrated in Fig. 5). Travel time predictions for a perfectly circular low velocity structure predict maximum travel time delay for the ray that travels along the diameter of the ULVZ (fully transmitted, with no refraction). This phase will travel along its great circle path. However, compared to the reference main phase at the stations, this postcursor arrival has a minimal delay time, as other rays that are refracted by the ULVZ have shorter paths within the ULVZ, but are more delayed with respect to the reference Sdiff due to their longer, out-of-plane paths. For an elliptically shaped ULVZ (rotated from the great circle path), the minimum travel time path is offset from the great circle path arrival, and the travel time move-out is asymmetric at both ends. Here it seems that a structure with a close-to-circular shape explains the travel time observations. The main indication of this comes from the fact that the minimally delayed postcursors of Event 1 arrive along the great circle path (Figs. 3 and 4). Furthermore, the minimal delay times of Events 1 and 2 lie within 10% of each other. On the other hand, there is some indication of slight asymmetry in the postcursor travel times on both sides of the minimum, especially in Event 2, so that the actual shape may be more elongated. However, the present data do not allow us to constrain the shape of the anomaly more precisely. Assuming a simplified 3D model also constrains the parameter space in which to search and illustrate trade-offs.

3.4. Forward modeling with CSEM

In order to interpret the full waveforms of the main phase and postcursors, we turn to an accurate but computationally heavy 3D numerical wave propagation method, the "sandwiched" version of CSEM (Coupled Spectral Element Method, Capdeville et al., 2002, 2003). Compared to other SEM codes (e.g. SPECFEM3D, Komatitsch and Tromp, 2002a, 2002b; Tromp et al., 2008) this

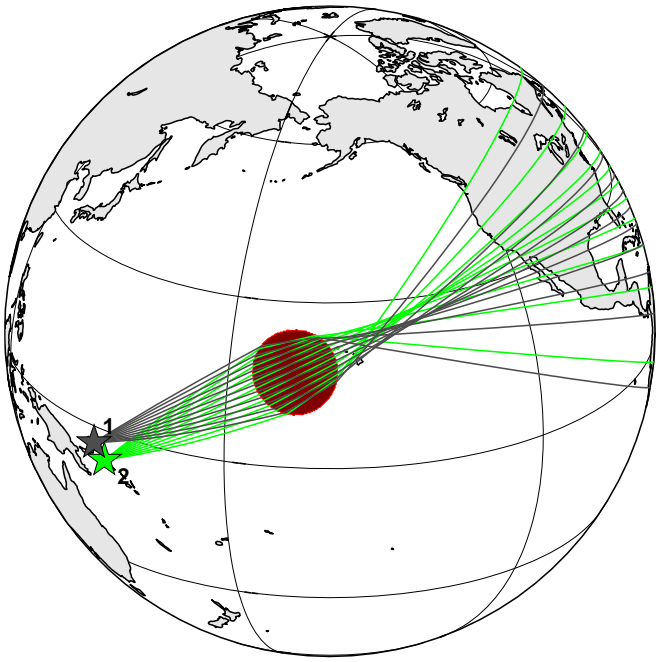

Fig. 5. Predicted behavior of infinite frequency rays as they become scattered by a ULVZ near Hawaii. Velocity reduction in the ULVZ is 20%. The focal point of the lens-like structure lies just beyond the structure.

method is computationally effective for the study of the D″ as it only solves for the full 3D spectral element solution in a layer of limited thickness (here 370 km) above the CMB. Details of the method are given in Supplementary material. We consider SAW24B16 (Mégnin and Romanowicz, 2000) as the background model in the SEM region for SH and SV. P velocity variations are scaled to the 1/3, and no density variations are implemented. Since SAW24B16 is a pure SH velocity model it agrees best with our SH observations modeled here. We did not test the possible effects of anisotropy in the D″ or upper mantle, but we expect the travel-time deviations of these complexities to be on the order of seconds. The only modifications made are that (1) the velocity model at 2800 km depth is extended down to the CMB and (2) in the top 70 km of the SEM region, SAW is smoothed towards PREM with a cosine taper. Additionally, the background velocity is reduced by 0.5% to best match the observations.

4. Results from forward modeling

4.1. Proposed preferred ULVZ

Our favorite model consists of a cylindrical ULVZ centered at 167.5°W and 17.5°N. It has a radius of 455 km, a height of 20 km and a velocity reduction of 20%. Therefore, the width:height ratio is around 45:1. The synthetic waveforms for all the three events are shown in Fig. 6. As a quantitative illustration, mean waveform correlation between synthetics and observed traces for diffracted phases of Event 1 is 0.07 for PREM, 0.43 for modified SAW24B16 (NZ) and it improves to 0.64 for our 3D ULVZ model (ZF2). The preferred model reproduces postcursor I with a similar move-out and slightly stronger amplitudes, especially at the lower distances. The model reproduces an amplitude reduction for Event 1 at the largest azimuths. This amplitude reduction extends to smaller azimuths in the observations. Results for a broader period range for Event 1 are shown in Fig. S7.

In the next sections we will show several tests that indicate the uncertainty in the parameters and some of the trade-offs between them. In the end we include Event 3 for additional azimuthal coverage. As our tests will illustrate, we are looking at rough uncertainties on the order of degrees in lateral location, ±5 km in height, ±100 km in lateral extension and several % in velocity reduction.

4.2. Trade-offs

4.2.1. Height

In the first test we investigate the influence of the height of the ULVZ by forward modeling with CSEM. The height is best constrained by the frequency dependence in the amplitudes of the observed main phase and postcursor I. We run tests for heights of 15, 25, 35 and 45 km for a model with 440 km radius, −20% shear velocity change and centered at 165°W and 19°N (models ZH1–ZH4, see Table 1). Fig. 7 shows waveforms for USArray station 933A at an azimuth of 62° and a distance of 108° for models with different heights. All traces in Fig. 7 are normalized by the same value. Two different period bands, 10–20 s and 10–30 s, are shown. Both the amplitude of the main phase and the move-out and shape of the postcursor are sensitive to the height of the ULVZ. In order to fit the observations, the amplitude of the main phase needs to be more reduced in the 10–20 s period band than in the 10–30 s period band. In the 10–20 s band, the amplitude of the main phase becomes smaller relative to the postcursor for the thicker models. The move-out of the postcursor increases with thickness, implying trade-off between thickness and velocity reduction. There is a similar move-out of the postcursor with thickness in the 10–30 s period band. In this period band, the amplitude of the main phase also decreases with thickness, but for thinner models, it is less affected than at shorter periods. In both period bands, the amplitudes and move-out agree best with a ~25 km thick model.

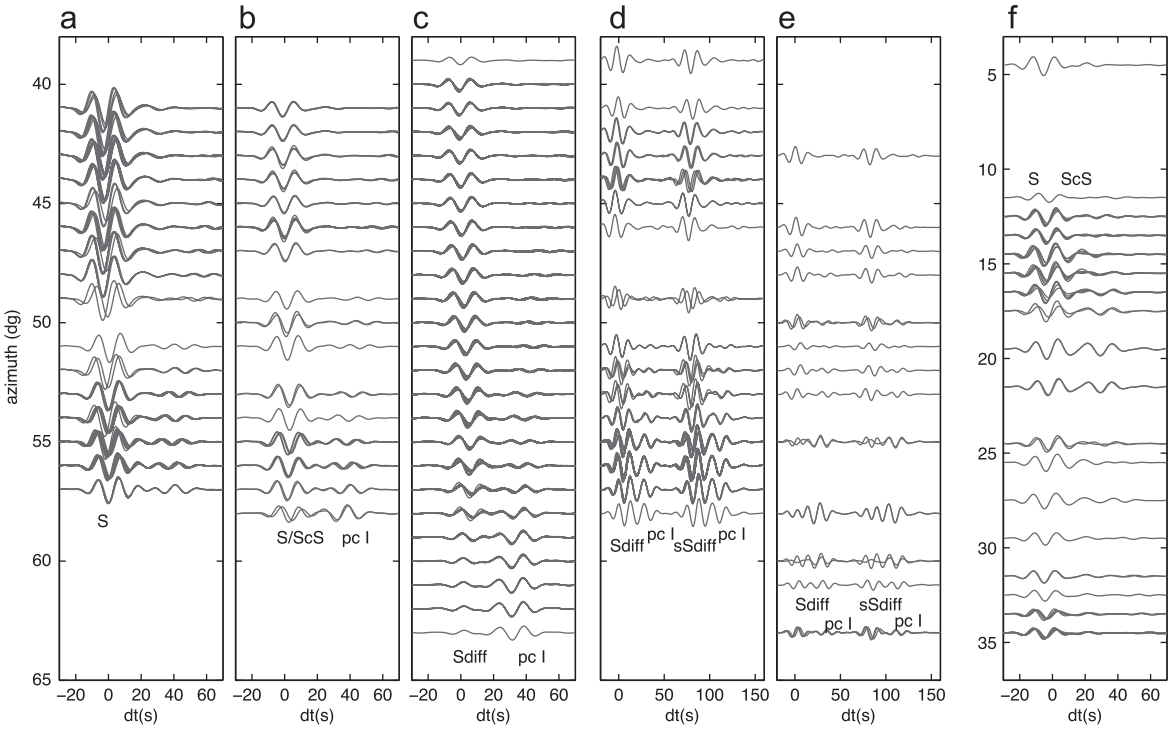

Fig. 6. Synthetic tangential waveforms for Event 1 at distances between 88° and 94° (a), 94° and 100° (b), and 100° and 110° (c), for Event 2 between 88° and 94° (d) and 94° and 110° (e) and for Event 3 between 89° and 96° (f). Panels can be directly compared with observed data in Fig. 2. (a) Event 1:S, (b) Event 1:S/ScS, (c) Event 1:Sdiff, (d) Event 2:S/ScS, (e) Event 2:S/Sdiff and (f) Event 3:S/ScS.

In order to get a sense of lateral variations of the height, we find the minimum RMS error at each station between the observed waveforms and the SEM synthetics for various heights. Postcursors at most azimuths come from a different direction than the main phase, so both phases sample different parts of the ULVZ. We therefore apply this procedure separately to the main phase and postcursor I by windowing. The resulting best fitting heights are plotted on a map in Fig. S8. For the postcursor, we find the best fits in the 10–20 s period band, as the main phase and postcursor are best separated at these shorter periods. For the main energy, we fit both the 10–20 s and 10–30 s period bands, to take full advantage of the difference in amplitude between these two frequency bands. Overall the 25 km model fits best, although there is some scatter that is difficult to interpret. Some of the scatter might be due to irregularities in the shape of the ULVZ, while other discrepancies might result from unmodeled attenuation and near-receiver effects. The move-out of the postcursor entails trade-offs with the lateral extent and velocity reduction of the model. The same test with a slightly stronger model (410 km radius and 25% velocity reduction) results in more stations preferring a 15 km thick model.

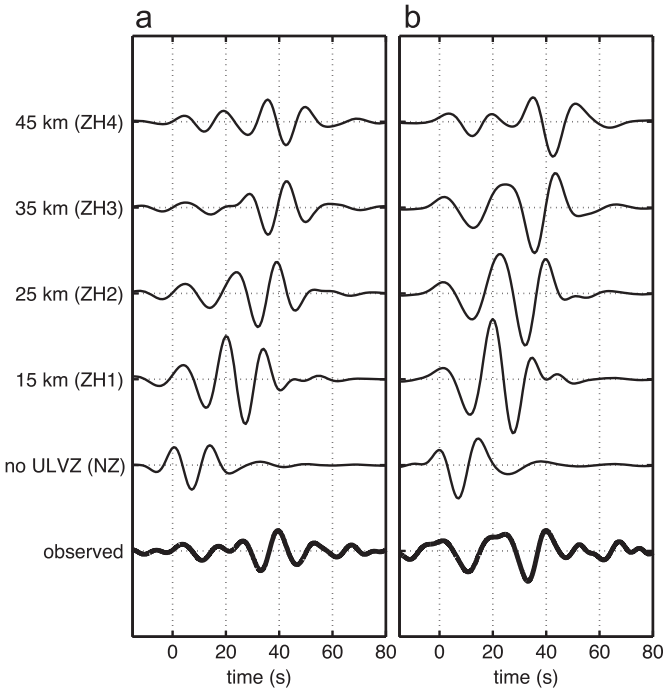

Fig. 7. Real and synthetic waveforms for station 933A of the Transportable Array at an azimuth of 62° and 108° for two different frequency bands (a: 10–20 s and b: 20–30 s). All traces are normalized by the same constant. Synthetic models (ZH1–ZH4) include a cylindrical ULVZ with a 440 km radius, 20% velocity reduction, and centered at 165°W and 19°N.

We can roughly compare the case of diffracted phases in a ULVZ on the CMB to surface waves sensing a low-velocity basin in the crust. The rule of thumb for the period band (T) of an SH wave sensitive to slow the shallow structure with a specific height (h) is given by $T = 4\,h/\beta$, where β is the shear velocity (Haskell, 1960). Applying this rule of thumb here, we note that the period band around 20 s is most affected by the ULVZ. At 20 s, a height of 27 km is predicted, very similar to what we find here by forward modeling.

4.2.2. Extent and velocity reduction of the ULVZ

Even within our simplified cylindrical model, a huge computational effort is required to grid search the range of possible sizes and velocity reductions or to apply a non-linear inversion algorithm. Here we gain our first estimate on these parameters from ray-theoretical predictions to reduce the search space. The estimated travel time delay for the path along the diameter of the ULVZ is given by $(2r/v)(1/((1-dv)/v)-1)$, where r is the radius of the structure at the CMB, dv is the velocity reduction, and v is the reference velocity inside the LLSVP. This delay time corresponds to the minimally delayed postcursor that travels along the great circle arc. The band between gray lines in Fig. 8a contours the minimal delay times between 30 s (minimal postcursor delay for Event 1, Section 3.1) and 32 s (for Event 2), illustrating the trade-off between the two parameters.

Next, we implement several models in CSEM and forward model waveforms for Event 1. Models ZS1–ZS4 are located at 165°W and 19°N and are 25 km in height (Table 1). The size and velocity reduction of these models are color-coded and plotted in Fig. 8a and the resulting travel time delays for postcursor I (scaled by amplitude) are shown in the following panel (Fig. 8b). The minimal delay times for the models in the gray band do not quite agree with the expected minimal delay times as predicted by ray theory. This is not surprising, as the finite-frequency sensitivity kernel of the wave is also sensitive to faster velocities above the ULVZ. In the previous section we also saw that increasing the

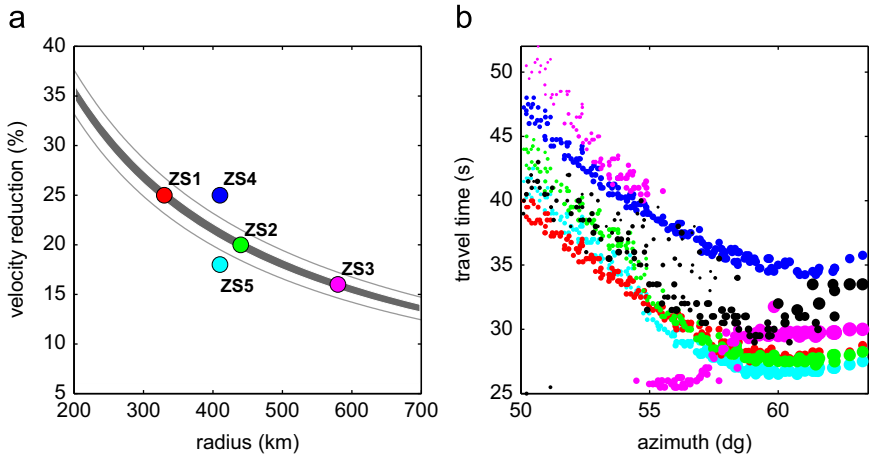

Fig. 8. (a) Trade-off between size and velocity reduction shown by the gray band, which represents ray-theoretical prediction times between 30 and 32 s. Colored dots show models implemented in CSEM. (b) Travel times for models implemented in CSEM as a function of azimuth (color coordinates with panel a). Size of the markers indicates amplitudes. Observed travel times and amplitudes are shown in black. (For interpretation of the references to color in this figure legend, the reader is referred to the web version of this article.)

height of the ULVZ increases the sensitivity of the phase and thus increases the delay of the postcursor. For the largest model (ZS3) we see the postcursors merge towards the main phase. The strongest postcursor in this case is the intermediate postcursor, postcursor II, which we introduce in Fig. S2. Waveforms for models ZS1–ZS3 are shown in Fig. S9. As the model size increases we see an increasing amplitude of the postcursor. And for the largest model, the waveforms make very clear that postcursor II becomes stronger than postcursor I. ZS4 and ZS5 are models that fall above and below the line in Fig. 8a, to illustrate the expected effect on the delay times.

Overall, to fit our observations (with this height), the model needs to be slightly above the gray band, while amplitudes of the postcursor are best fit for a radius around 400 km ($\pm$100 km) at the CMB. To fit just Event 1 we could settle for a model with a radius of 455 km and a velocity reduction of 20%.

4.2.3. Location of the ULVZ

We investigate the possible locations by predicting ray-theoretically where the postcursor with minimum delay should arrive. When assuming a circular-base, the minimally delayed postcursor travels (non-refracted) through the center of the ULVZ along the great circle path.

Event 1 has a minimal travel time around 60° azimuth, while Event 2 has a minimal travel time around 57° azimuth (Section 3.1). We grid search over the area around the diffracted paths allowing for some uncertainty in these azimuth values. Fig. 9 shows the bands of possible ULVZ centers for a two degree uncertainty (dark green) and a one degree uncertainty (green). The spread in possible locations is strongly anisotropic, being poorly constrained along the direction of propagation, and well constrained perpendicular to this direction. Next we model several models within this area. All models, ZL1–ZL5, have the same size (455 km in radius), velocity reduction (20%) and height (25 km). The circular bases for five locations are colored in Fig. 9. Waveforms of these models for Event 1 are plotted in Fig. S10 for those traces where the postcursor is strong (azimuth $>50°$, $100° <$ dist $<110°$). As the model shifts further to the west, part of it lies outside the diffracted path, and postcursor I becomes weaker. ZL3–ZL5, which are further to the east, correlate better with the observed data. It is difficult to distinguish between these three models on the basis of just one event.

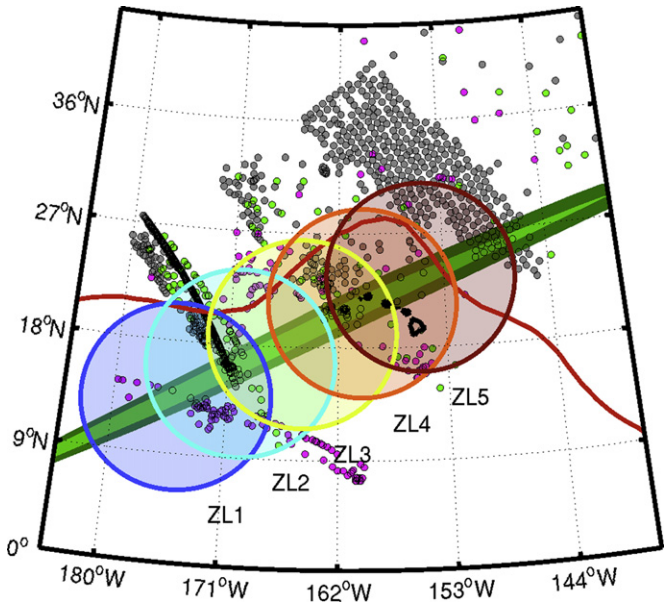

Fig. 9. Grid search results for the center of a circular ULVZ that fit the minimal delay times of postcursor I in the ray-theoretical limit. Best locations are in the green band, while other reasonable locations are in dark green. Colored dots show coverage of Event 1 (gray), Event 2 (green) and Event 3 (magenta). Circular bases of the tested models ZL1–ZL5 are plotted and color-coded. Red line indicates LLSVP boundary in SAW24b16 at a depth of 2750 km. (For interpretation of the references to color in this figure legend, the reader is referred to the web version of this article.)

Additional constraints come from Event 3. Even though Event 1 prefers a model more to the east, it strongly favors a ULVZ model located further to the west as this is where the phases are most strongly scattered. From the coverage of Event 3 (magenta in Fig. 9), it already becomes clear that most of the traces of Event 3 will hardly be affected by the easternmost models. Synthetic waveforms for this event are computed with a ULVZ centered at (165°W , 19°N) and (170°W , 16.5°N), respectively, ZL2 and ZL3, and one model (ZF1) in between at (167.5°W , 17.5°N). Waveforms are compared to the observations in Fig. S11. The location further to the west better predicts the strongest scattering of the waveforms around azimuths of 12–20°. The intermediate model, ZF1, fits best without strongly reducing the fit to Event 1. The finalized location at 167.5°W and 17.5°N is centered about 11° to the southwest of Hawaii. To improve the travel time and amplitude fits of Event 3, the model is also reduced to 20 km in height (ZF2), without reducing the fits to Event 1. This results in the proposed model as presented in Section 4.1 and Fig. 6. Only around an azimuth of 20° does our model produce some postcursors that are not observed in the data.

Fig. 3a shows the travel times of the proposed model on top of the observed ones. The model does well in fitting the travel time move-out in the main phase as it enters the LLSVP and ULVZ at higher azimuths. The move-out of the postcursor is slightly stronger in the synthetics. Above 60°, both the main phase and the postcursor are more delayed in the observations, which can be due to the source or receiver side of the path. Fig. 4 compares the beamforming results for synthetic models ZF2 and ZL4 to those observed. ZL4, located more to the northeast, does a better job explaining the backazimuth deviation of the postcursor between 55° and 63°. Model ZF2 performs better at azimuths between 50° and 55°. Additionally, the location of ZF2, as constrained by Event 3, cannot be ruled out, as additional focusing could be accounted for by a non-circular ULVZ boundary or other 3D heterogeneity on the Sdiff path beyond the ULVZ, possibly the LLSVP boundary. Additional focusing of the scattered rays, would also account for a more moderate move-out in the postcursor travel times (Fig. 3a).

5. Discussion

The Sdiff phase is not commonly used to detect ULVZs, but as these events illustrate, Sdiff can be strongly affected by ULVZs. In the diffracted part of the phase, it is sensitive to wide structures, like the ULVZ modeled here. The strong effects on the amplitude reduction and strongly delayed postcursor are clearly visible by eye. On the downside, diffracted phases give an integrated sensitivity to the diffracted part, lacking along path resolution (similar to surface waves), and resulting in trade-offs. As shown here, the strongest uncertainty lies in the location, when azimuthal coverage is limited.

The postcursor delay is modeled in reference to the main phase. As the main phase and postcursor have different paths in the D″ there is uncertainty caused by smaller complexities in the ULVZ boundary, velocity gradients within the ULVZ, additional small, slow structures in other parts of the path, CMB topography, the details on the LLSVP boundary and anisotropic velocities. We expect these effects to be on the order of seconds causing the observed scatter in postcursor delay times. Some of these complexities, and unmodeled effects of attenuation, could also explain

the stronger decrease in the observed main phase amplitude compared to the synthetics.

The southern boundary of a ULVZ was previously detected in the area studied here through scattering in PKP waves (Luo et al., 2001). Most of the area of our preferred model is located north of this boundary, but the southern end extends across their boundary. Our data coverage does not extend far enough south to see this boundary in the direct phases. However, postcursors from the southernmost part of the ULVZ do diffract northwards and arrive at shorter distances. As the amplitudes of the postcursors at these shorter distances are too strong in the synthetics, this boundary might be more irregular, or not extend as far south as presented here.

Our final model also differs from previous Sdiff postcursor modeling for this region. To et al. (2011) modeled Event 2 combined with an event in 1997. Both these events occurred before the deployment of the Transportable Array and thus coverage was limited. To et al. (2011) modeled the postcursors for a 2D case with a ULVZ embedded in a low velocity zone. Their modeling, however, was restricted to a 2D great circle plane. Their 2D ray-tracing proposed a main phase that travels above the ULVZ, while the postcursor diffracts within the ULVZ and is thus delayed. In contrast, we assume that the two phases split due to different sensitivities in the vertical plane as a function of frequency. With the denser coverage of Event 1, it becomes apparent that the amplitude of the main phase at periods shorter than 30 s is reduced, while longer periods are less affected. This leads us to propose a much thinner model ($\sim$20 km versus $\sim$80 km).

We note that the Pdiff phases in the 10–20 s band for Event 1 show move-out towards the south (Supplementary material Section 3) when entering the LLSVP, but show no further delay due to the ULVZ. This suggests a weaker P velocity reduction, reinforcing the suggestion of a distinct chemical nature or the occurrence of partial melt. However, modeling the exact P velocity reduction is complicated by the strong trade-off with the unknown velocity reduction in the LLSVP in which the ULVZ is embedded. The present data do not provide any constraints on the density within the ULVZ. Synthetic waveforms for the model do not change when density is increased by 20% within the ULVZ. We also note that, although this ULVZ has a large lateral extent, it is not detected in tomographic models because of its small height.

The location of the ULVZ is close to the northern boundary of the Pacific LLSVP. One of the mechanisms proposed for a possible correlation of ULVZs with LLSVP boundaries is that dense chemically distinct material is dragged and accumulated along the edges of upwelling zones. It generally takes on ridge-like shapes in numerical simulations (McNamara et al., 2010). Here, our best model is cylindrical, but even though we tried some ridge-like features without much success, uncertainty on the precise shape remains. The discrepancy in preferred location between Events 1 and 3 argues for a more elongated shape parallel to the LLSVP boundary.

There are also possible correlations between both ULVZs and LLSVP boundaries with hotspots (Torsvik et al., 2006). So far seismological studies do not agree whether whole mantle plumes exist and if yes, whether a whole mantle plume lies directly below the Hawaiian hotspot or is offset somewhere within the mantle (Cao et al., 2011; Wolfe et al., 2011). It is tempting to speculate on the relationship of the unusually large ULVZ found here in close vertical proximity with the hotspot with the largest plume flux (Sleep, 1990; Jellinek and Manga, 2004). If this were the anchor of a long-lived whole-mantle plume, then the plume could be tilted upward to the ENE in the lower mantle. Alternatively, upwelling material could pond at the mantle transition zone and offset further to the east (Cao et al., 2011). Geochemical signature from Hawaiian islands shows an enrichment in Fe (Humayun et al., 2004) and an Os isotope signature (Brandon et al., 1998) for which one possible explanation is the interaction with the outer core at the CMB. Entrainment from the ULVZ might be a source for the increased isotopic heterogeneity measured in lavas on the southwestern side compared to lavas on the northeastern side of the Hawaiian chain (Abouchami, 2005; Weis et al., 2011).

6. Conclusions

The move-out, amplitude decrease and postcursors observed in shear waves crossing the deep mantle beneath the Central Pacific can be well explained by a ULVZ embedded within the LLSVP. The ULVZ width of our preferred model is $\sim$910 km at the CMB, with a velocity reduction of $\sim$20%, but some trade-off exists between these two parameters. This is the first time it is possible to provide a constraint on the lateral extent of a ULVZ with some precision. The cylindrical model is centered around 172.5°W and 162.5°N. Although its location is somewhat uncertain, the ULVZ sits close to the northern border of the Pacific LLSVP and to the southwest of the Hawaiian hotspot. The height of 20–25 km is the best constrained parameter due to the frequency dependence of the main phase and postcursor amplitude and separation. Whatever the relationship of the ULVZ to the Hawaiian hotspot, the geometry of the mapped structure needs to be taken into account in geodynamics and mineral physics studies of the deep mantle.

Acknowledgments

We thank Akiko To for helpful discussions. This work was supported by NSF/CSEDI grant # EAR-167513 and ERC grant 'WAVETOMO'.

Appendix A. Supplementary data

Supplementary data associated with this article can be found in the online version at http://dx.doi.org.10.1016/j.epsl.2012.09.005.

References

Abouchami, W., 2005. Lead isotopes reveal bilateral asymmetry and vertical continuity in the Hawaiian mantle plume. Nature 434, 837–840.
Bower, D., Wicks, J., Gurnis, M., Jackson, J., 2011. A geodynamic and mineral physics model of a solid-state ultralow-velocity zone. Earth Planet. Sci. Lett. 303 (3–4), 193–202.
Brandon, A., Walker, R., Morgan, J., Norman, M., Prichard, H., 1998. Coupled 1860s and 1870s evidence for core–mantle interaction. Science 280 (5369), 1570–1573.
Cao, Q., van der Hilst, R., de Hoop, M., Shim, S., 2011. Seismic imaging of transition zone discontinuities suggests hot mantle west of Hawaii. Science 332 (6033), 1068–1071.
Capdeville, Y., Larmat, C., Vilotte, J., Montagner, J., 2002. A new coupled spectral element and modal solution method for global seismology—a first application to the scattering induced by a plume-like anomaly. Geophys. Res. Lett. 29, 1318–1322.
Capdeville, Y., To, A., Romanowicz, B., 2003. Coupling spectral elements and modes in a spherical earth: an extension to the sandwichcase. Geophys. J. Int. 154 (1), 44–57.
Clayton, R., Trampert, J., Rebollar, C., Ritsema, J., Persaud, P., Paulssen, H., Prez-Campos, X., VanWettum, A., Prez-Vertti, A., DiLuccio, F., 2004. The NARS-Baja seismic array in the Gulf of California rift zone. MARGINS Newslett. 13, 1–4.
Davaille, A., 1999. Simultaneous generation of hotspots and superswells by convection in a heterogeneous planetary mantle. Nature 402, 756–760.
Deschamps, F., Kaminski, E., Tackley, P., 2011. A deep mantle origin for the primitive signature of ocean island basalt. Nat. Geosci. 4, 879–882.
Dziewonski, A., Anderson, D., 1981. Preliminary reference earth model. Phys. Earth Planet. Int. 25 (4), 297–356.
Dziewonski, A., Lekic, V., Romanowicz, B., 2010. Mantle anchor structure: an argument for bottom up tectonics. Earth Planet. Sci. Lett. 299, 69–79.
Haskell, N., 1960. Crustal reflection of plane SH waves. J. Geophys. Res. 65 (12), 4147–4150.
He, Y., Wen, L., 2009. Structural features and shear-velocity structure of the pacific anomaly. J. Geophys. Res. 114, B02309.

Hier-Majumder, S., 2008. Influence of contiguity on seismic velocities of partially molten aggregates. J. Geophys. Res. 113, B12205.
Humayun, M., Qin, L., Norman, M., 2004. Geochemical evidence for excess iron in the mantle beneath Hawaii. Science 306 (5693), 91–94.
Ishii, M., Tromp, J., 2004. Constraining large-scale mantle heterogeneity using mantle and inner-core sensitive normal modes. Phys. Earth Planet. Int. 146 (1–2), 113–124.
Jellinek, A., Manga, M., 2004. Links between long-lived hot spots, mantle plumes, d″, and plate tectonics. Rev. Geophys. 42, RG3002.
Koelemeijer, P.J., Deuss, A., Trampert, J., 2012. Normal mode sensitivity to Earth's d″ layer and topography on the core–mantle boundary: what we can and cannot see. Geophys. J. Int. 190 (1), 553–568.
Komatitsch, D., Tromp, J., 2002a. Spectral-element simulations of global seismic wave propagation. I. Validation. Geophys. J. Int. 149 (2), 390–412.
Komatitsch, D., Tromp, J., 2002b. Spectral-element simulations of global seismic wave propagation. II. Three-dimensional models, oceans, rotation and self-gravitation. Geophys. J. Int. 150 (1), 303–318.
Luo, S., Ni, S., Helmberger, D., 2001. Evidence for a sharp lateral variation of velocity at the core–mantle boundary from multipathed PKPab. Earth Planet. Sci. Lett. 189 (3–4), 155–164.
Mao, W., Mao, H., Sturhahn, W., Zhao, J., Prakapenka, V., Meng, Y., Shu, J., Fei, Y., Hemley, R., 2006. Iron-rich post-perovskite and the origin of ultralow-velocity zones. Science 312 (5773), 564–567.
McNamara, A., Garnero, E., Rost, S., 2010. Tracking deep mantle reservoirs with ultra-low velocity zones. Earth Planet. Sci. Lett. 299, 1–9.
McNamara, A., Zhong, S., 2004. Thermochemical structures within a spherical mantle: superplumes or piles. J. Geophys. Res. 109, B07402.
McNamara, A., Zhong, S., 2005. Thermochemical structures beneath Africa and the Pacific ocean. Nature 7062, 1136–1139.
Mégnin, C., Romanowicz, B., 2000. The three-dimensional shear velocity structure of the mantle from the inversion of body, surface and higher-mode waveforms. Geophys. J. Int. 143 (3), 709–728.
Ni, S., Helmberger, D., 2003. Seismological constraints on the South African superplume; could be the oldest distinct structure on Earth. Earth Planet. Sci. Lett. 206 (1–2), 119–131.
Ni, S., Tan, E., Gurnis, M., Helmberger, D., 2002. Sharp sides to the African superplume. Science 296 (5574), 1850–1853.
Rondenay, S., Fischer, K., 2003. Constraints on localized CMB structure from multichannel, broadband SKS-coda analysis. J. Geophys. Res. 108, 2537–2553.
Rost, S., Garnero, E., Stefan, W., 2010. Thin and intermittent ultralow-velocity zones. J. Geophys. Res. 115, B06312.
Rost, S., Garnero, E., Williams, Q., 2006. Fine-scale ultralow-velocity zone structure from high-frequency seismic array data. J. Geophys. Res. 111, B09310.
Rost, S., Garnero, E., Williams, Q., Manga, M., 2005. Seismological constraints on a possible plume root at the core–mantle boundary. Nature 435 (7042), 666–669.
Sleep, N., 1990. Hotspots and mantle plume: some phenomelogy. J. Geophys. Res. 95, 6715–6736.
Steinberger, B., Torsvik, T., 2012. A geodynamic model of plumes from the margins of large low shear velocity provinces. Geochem. Geophys. Geosyst. 13, Q01W09.
Sun, D., Helmberger, D., Ni, S., Bower, D., 2009. Direct measures of lateral velocity variation in the deep Earth. J. Geophys. Res. 114 (B5), B05303.
Tan, E., Leng, W., Zhong, S., 2011. On the location of plumes and lateral movement of thermochemical structures with high bulk modulus in the 3-d compressible mantle. Geochem. Geophys. Geosyst. 12, Q07005.
Thorne, M., Garnero, E., 2004. Inferences on ultralow-velocity zone structure from a global analysis of SPDKS waves. J. Geophys. Res. 109, B08301.
To, A., Capdeville, Y., 2011. Constraints on the 3d shape of the ultra low shear velocity zone at the base of the mantle beneath the Central Pacific. AGU 2011 Fall Meeting San Francisco, December 5–9, DI43A–2082.
To, A., Fukao, Y., Tsuboi, S., 2011. Evidence for a thick and localized ultra low shear velocity zone at the base of the mantle beneath the Central Pacific. Phys. Earth Planet. Int. 184, 119–133.
To, A., Romanowicz, B., Capdeville, Y., Takeuchi, N., 2005. 3D effects of sharp boundaries at the borders of the African and Pacific superplumes: observation and modeling. Earth Planet. Sci. Lett. 233 (1–2), 1447–1460.
Torsvik, T., Smethurst, M., Burke, K., Steinberger, B., 2006. Large igneous provinces generated from the margins of the large low-velocity provinces in the deep mantle. Geophys. J. Int. 167 (3), 1447–1460.
Trampert, J., Deschamps, F., Resovsky, J., Yuen, D., 2004. Probabilistic tomography maps chemical heterogeneities throughout the lower mantle. Science 306 (5697), 853–856.
Tromp, J., Komattisch, D., Liu, Q., 2008. Spectral-element and adjoint methods in seismology. Communications in Computational Physics 3 (1), 1–32.
Weis, D., Garcia, M., Rhodes, J., Jellinek, M., Scoates, J., 2011. Role of the deep mantle in generating the compositional asymmetry of the Hawaiian mantle plume. Nat. Geosci. 4, 831–838.
Wicks, J., Jackson, J., Sturhahn, W., 2010. Very low sound velocities in iron-rich (Mg, Fe)O: implications for the core–mantle boundary region. Geophys. Res. Lett. 37, Art. No. L15304.
Williams, Q., Garnero, E., 1996. Seismic evidence for partial melt at the base of Earth's mantle. Science 273 (5281), 1528–1530.
Wolfe, C., Solomon, S., Laske, G., Collins, J., Detrick, R., Orcutt, J., Bercovici, D., Hauri, E., 2011. Mantle p-wave velocity structure beneath the Hawaiian hotspot. Earth Planet. Sci. Lett. 303 (3–4), 267–280.